SUPPLEMENTARY INFORMATION

S1. Age model

We developed an age model for core U1357B based on 87 ^{14}C analyses on bulk organic carbon (Fig. S1). In the standard IODP CSF-A depth scale, recovery often exceeds 100% and to correct for this, the standard IODP procedure is to apply a linear compression algorithm which is based on the assumption that expansion is uniform in the core. However, in U1357B, expansion due to biogenic gas was particularly high and resulted in discrete sections of core being pushed apart creating voids in the depth scale that did not represent real gaps in the stratigraphy. To account for this, the voids are numerically removed and depth scale adjusted prior to linear compression being applied (if recovery still exceeds 100%).

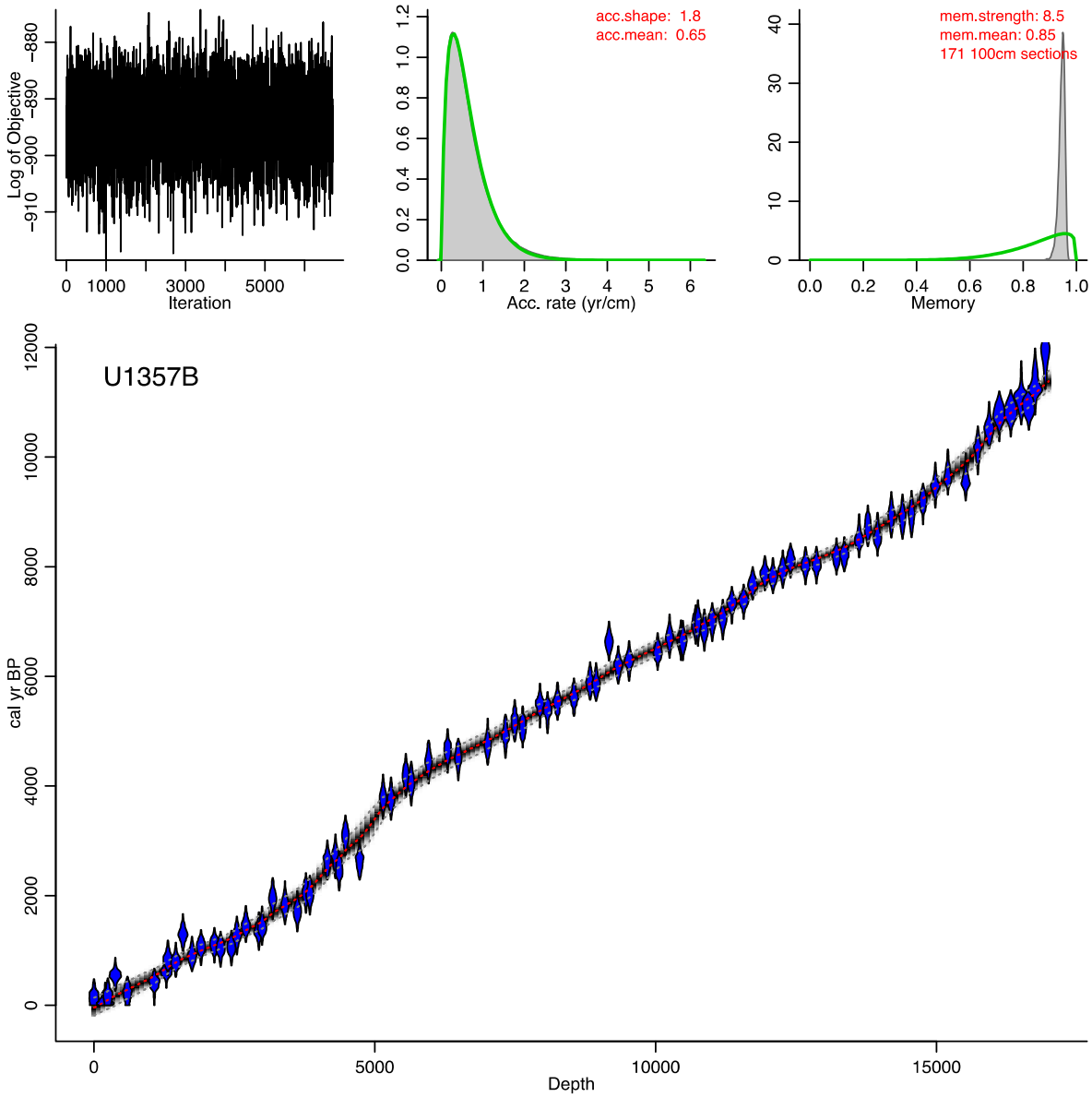

Figure S1. Age-depth plot of U1357B, using the default outputs from the BACON software. Upper panels show (from left to right): a stationary distribution of the Markov Chain Monte Carlo iterations; prior (green curve) and posterior (grey curve) distribution for the accumulation rate; prior (green curve) and posterior (grey curve) distribution for memory. Bottom panel shows the calibrated ^{14}C dates (blue) and age depth model with 95% confidence intervals.

The model was calibrated with a reservoir age correction of 1200±100 years and depth to age conversions achieved by using BACON. This is a Bayesian iteration scheme that invokes memory from dates above any given horizon, and produces a weighted mean and median age-depth curve (Blaauw and Christeny, 2011). The top depth of 3 m is consistent with the reservoir age in the Southern Ocean (Hall et al., 2010). Bulk organic carbon ages in the Antarctic are commonly

compromised by reworking of older carbon in the sediment column (Andrews et al., 1999), which is compounded by extreme sediment starvation of post-LGM sequences in the Antarctic. However, due to extremely high input of autochthonous carbon associated with the Adélie Drift deposit, which is a predominately seasonally deposited

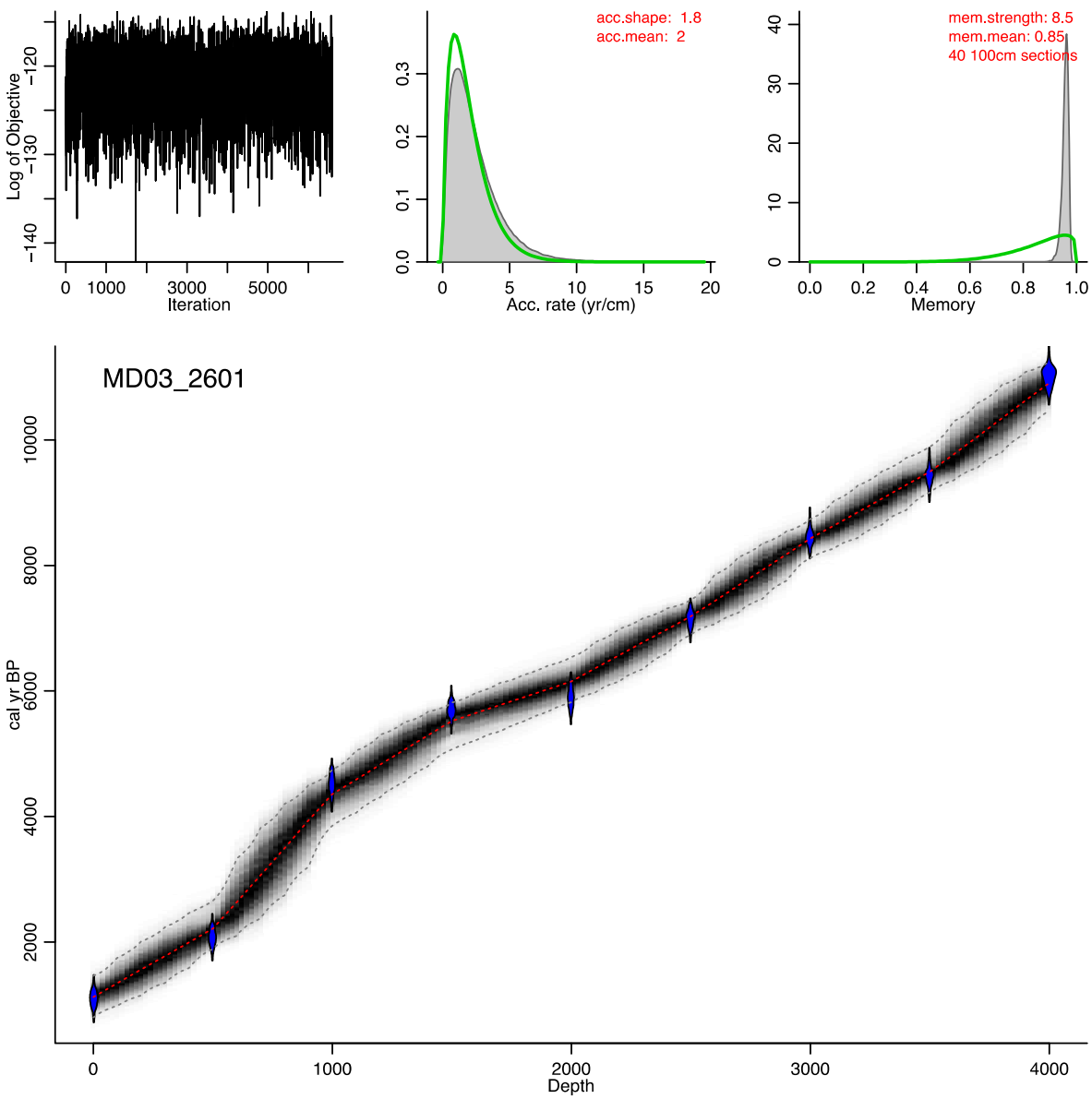

Figure S2. Age-depth plot of MD03-2601, using the default outputs from the BACON software. Upper panels show (from left to right): a stationary distribution of the Markov Chain Monte Carlo iterations; prior (green curve) and posterior (grey curve) distribution for the accumulation rate; prior (green curve) and posterior (grey curve) distribution for memory. Bottom panel shows the calibrated ^{14}C dates (blue) and age depth model with 95% confidence intervals.

diatom bloom, this reworking is expected to be minimal at the U1357 site, and is only a potential issue at the base of the core (Unit II), due to increased proximity to glacial influences from the Adélie Land coast during the deglaciation (e.g. > 11.4 ka). This is supported by the radiocarbon ages, maintaining a strong stratigraphic order (within error), relatively consistent sedimentation rates

throughout the deposited interval, and core top ages that are consistent with the expected reservoir age.

We also recalibrated the age-model for MD03-2601 applying the BACON methodology using the ^{14}C dates presented in (Crosta et al., 2008) (Fig. S2). This age model differs from that of (Denis et al., 2009a), who discarded two ^{14}C ages bracketing the mid-Holocene (4.4 and 5.6 cal ka BP), on the basis of an inferred meteorite impact at ca. 15 m and correlated this to an event at 4 ka BP. We note that this impact correlation does not provide a unique absolute age constraint, with our revised age model instead indicating an age of 5.4 cal ka BP for this impact event. Critically, comparison between the age model for U1357B and the revised age model for MD03-2601 now indicates a strong similarity regarding changes in the sedimentation rates at ca. 4.5 ka and ca. 2 ka BP, indicating that both sites are influenced by similar depositional processes.

S2. Further details on interpretation of proxy data

S2.1 Ba/Ti ratio excess as a primary productivity proxy

Ba-based proxies (e.g., Ba/Ti or equivalent Ba/Al) in the Wilkes Land margin sediments have been commonly related to marine productivity (Presti et al., 2011), although studies in other pelagic environments indicate that they can also be sensitive to bottom current intensity (Bahr et al., 2014), meltwater (Plewa et al., 2006), and other processes (Griffith and Paytan, 2012). FESEM analysis and images at Site U1357 indicate the presence of biogenic barite (Fig. S3a), recognized by the elliptical morphologies and sizes between 1 to 3 μm (Paytan et al., 2002). Titanium is found associated with small heavy minerals (ilmenite) with angular and low sphericity shapes.

Along the entire record, Ba/Ti ratios show persistent periodic fluctuations with values between 0.1 and 2.7. Nevertheless, a marked enrichment can be observed at 4.5 ka reaching Ba/Ti ratio values over 36.1 (Fig. 2). Pore water analysis indicates that the carbon dioxide (methanic) reduction zone

(CRZ) is reached just few cm near sea floor and the upper 20 m already contain sulfate-free interstitial waters (Escutia et al., 2011). Observed geochemical conditions indicate that some Barite dissolution could be expected, but there is no diagenetic barite that could justify the obtained enrichment. In addition, at the enriched interval we did not observe any lithological change or enrichment in other elements (e.g., Si). The influence of aeolian dust or fluvial input on Ba input can also be discarded in the glaciated Wilkes Land margin. In the same way, Ba concentration in sea-ice is considered null because on an annual cycle, sea ice does not constitute a net source or sink of these species to the underlying seawater (Thomas, 2011).

Furthermore, FESEM imaging detected biogenic barite during intervals were the Ba/Ti excess occurs (Fig. S3) pointing to an increase in productivity. This may be driven by water column stratification

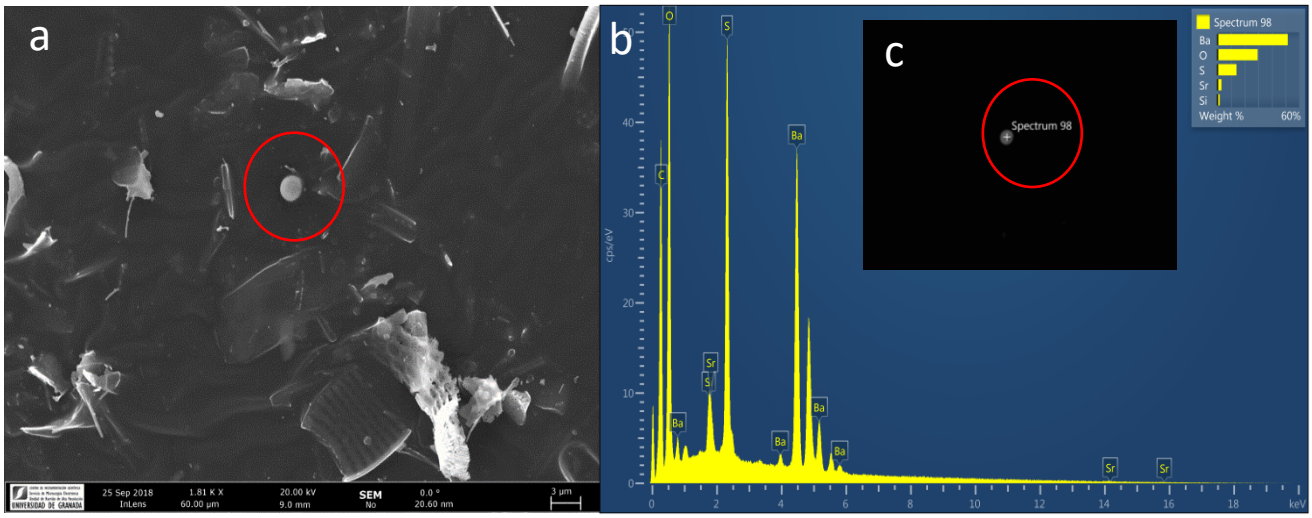

Figure S3. Authigenic marine barite (red circle, size > 300nm) observed in Ba/Ti enriched interval (sample U1357B-8H-2A 141-143; age: 4,430 cal yr) a) SEM image obtained with secondary electrons with Inlens detector at 20 kV b) SEM-EDX spectrum (analyzed spot marked with a white cross in image c)) showing barite composition ($BaSO_4$) c) Same barite shown in a backscattered electron (BSE) mode by AsB detector at 20 kV.

or greater nutrient availability. This interpretation is coherent with other paleoproductivity reconstructions in this area, in particularly peaks in ^{230}Th-normalized fluxes of biogenic silica (BSi) and organic carbon content recorded in nearby core MD03-2601 (Denis et al., 2009b) (when using the recalibrated age-model – see S2).

S2.2 Grain size

Grainsize analysis was conducted on paired samples with lipid biomarker samples in Unit I. Unit I represents the onset of the modern deposition at Site U1357, and the underlying stratigraphy is discussed in the main text. Between ca. 11.4 and 8 ka, U1357B has a relatively high terrigenous component (i.e. high Natural Gamma Radiation (NGR) content and low BSi%; Fig S4). The grain size distribution contains coarse tails of fine (125-250 μm) to medium sands (250-500 μm), but only one sample contains coarse sands (>500 μm) that may represent ice-berg rafted debris (IBRD). However, terrigenous content and IBRD is more common in the underlying Unit II, which is interpreted to represent a true "calving bay environment" (Escutia et al., 2011). Shipboard description of the core faces found the presence of small isolated facetted and striated pebbles (lonestones) in Unit II (Escutia et al., 2011), which is supportive of an iceberg component to sediment supply, but these are largely absent in Unit I. The fine grained sands and muds have a distribution with similar modes to overlying intervals, albeit with an increase in the size of the coarse silt and very fine sand modes. The subtle increased sorting up core between ca. 11.4 and ca.8 ka (from very poorly to poorly sorted, Fig. S4) is consistent with an increasingly more distal setting, with less potential for a glacial grounding line sediment supply (Powell and Domack, 1995; McKay et al., 2009). This interval is interpreted to reflect the final post-LGM retreat of local EAIS outlet glacier grounding lines from a proximal (less sorted, more IBRD) to more distal setting (better sorted, less IBRD) from the site, although we note a much larger shift occurs at the Unit I/II boundary at 170.25 mbsf (ca.11.4 ka) (Escutia et al., 2011) and dominant sediment supply from local outlet glaciers probably ceased at this earlier time. It is likely this distal setting was close to the modern day grounding line, as the Dumont d'Urville Trough is overdeepened between Site U1357 and the modern day grounding line, and this bathymetry configuration is inherently unstable for marine-based ice sheets (Thomas and Bentley, 1978; Bentley et al., 2014).

Today, Adélie Land glaciers are inferred to have relatively clean basal layers due to the solid bedrock (Kleinschmidt and Talarico, 2000), and distal polar glacimarine settings are usually sediment starved and provide very low inputs of terrigenous sediments (Powell and Domack, 1995; McKay et al., 2009).

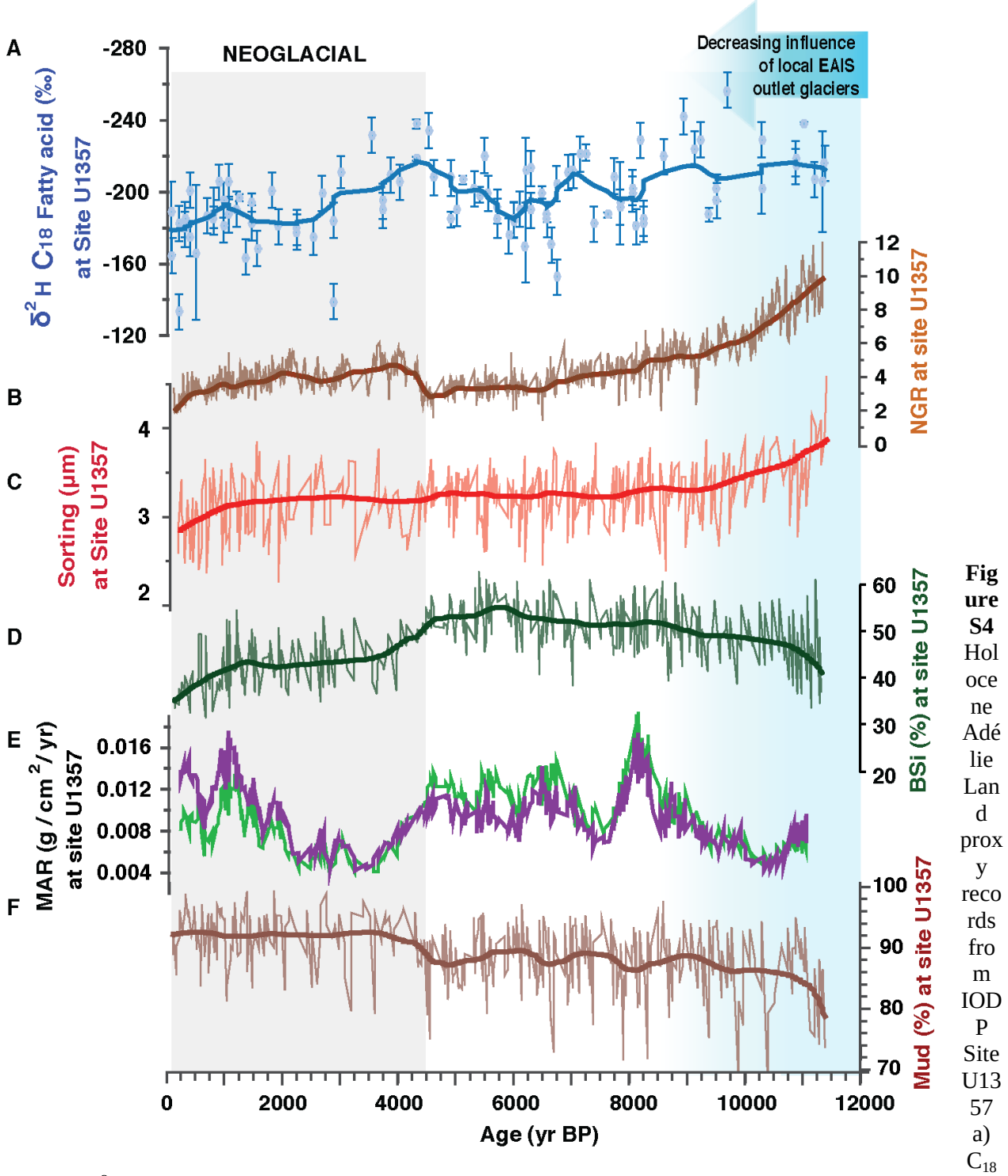

Figure S4 Holocene Adélie Land proxy records from IODP Site U1357 a) C_{18} fatty acid δ^2H (errors bars based on replicate analyses), heavy line is a robust locally weighted scatterplot smoothing (rlowss) b) Natural Gamma Radiation, heavy line is a rlowss c) grain sorting (µm) calculated following Folk and Ward (1957), heavy line is a rlowss d) Percentage of biogenic silica (BSi), heavy line is a rlowss; e) Mass accumulation rates of biogenic (green line) and terrigenous (purple line) material f) Percentage of mud, heavy line is a rlowss.

There are also no large proglacial fans evident at the mouths of these glaciers (Beaman et al., 2011) and consequently, direct sediment discharge from the Mertz and Ninnis Glaciers is unlikely to be of significant quantity to sustain dense overflows delivering sediment over the Adélie Bank and into the Dumont d'Urville Trough. Therefore, the release of terrigenous material through glacial melting is low (to absent) when glacier activity is steady and distal from the site, but is anticipated to increase

with increased proximity to the glacier front or with enhanced dynamic ice discharge (which may occur either during a retreat or advance), which would be associated with an increase in IBRD from local outlet glaciers. We note evidence for proglacial fan deposition and IBRD is lacking throughout Unit I (post 11.4 ka).

Between 9 and 4.5 ka, mass accumulation rates (MARs) (both biogenic and terrigenous; Fig. S4) are relatively high, albeit with millennial scale variability. However, the mean grain size and sorting of the terrigenous material is relatively stable throughout the entire interval, and as with the rest of Unit I there is an almost complete lack of IBRD. This suggests that sediment input from grounding line processes were also minimal through this time. Based on the drift morphology (Fig S5), and the prevailing easterly flow of the Antarctic Coastal Current, this interval is interpreted to be the result of sediment advection to the site from the east as residual ice retreated from the bathymetric highs in the region. Diatom frustules and sponge spicules are mainly in the 16 to 63 μm range, much of which is maintained in suspension by weak currents (a few cms^{-1}) (Dunbar et al., 1985). The greater area of open water for primary production during the summer, combined with an open pathway for advection of biogenic matter from the MGP (Fig. 1) can thus explain the significant rise in linear sedimentation and mass accumulation rates for both biogenic and terrigenous material. Most of the terrigenous material after ~8 ka is proposed to have been primarily eroded off the Adélie Bank by westward flowing currents into the Adélie drift where sediment would have settled out from suspension. Terrigenous sediment younger than 8 ka in this drift is almost entirely finer than 125 μm, while Dunbar et al. (1985) revealed that surface sediments on shallow banks have a grain size distribution that generally exceeds 125 μm. This supports our interpretation that the majority of the terrigenous material in U1357B is winnowed from these banks by bottom currents. The size of the material winnowed implies that maximum current velocities in the region are greater than 18-20 cm s^{-2}, the minimum velocity required to transport fine sand by intermittent suspension and suspension in poorly sorted glacimarine settings (Singer and Anderson, 1984; McCave and Hall, 2006).

The complete lack of medium to coarse sand in the grainsize distributions of Unit I (<11.4 ka), and from visual observation of the core face, that may represent IBRD may be the consequence that icebergs calved from large ice shelves and ice tongues, such as the RIS and Mertz Glacier Tongue, are advected into the region via the Antarctic Coastal Current but usually lack basal debris. While the lack of IBRD could in part be explained as the consequence of the widespread development of the RIS in the Holocene (McKay et al., 2016), it could also be due to the Adélie and Mertz Banks (and Mertz Glacier Tongue) acting to shield Site U1357 from large icebergs passing over the site, as icebergs would have become grounded on the bathymetric highs and deflected north (Massom et al., 2001; Beaman et al., 2011). Notably, this lack of IBRD further supports a lack of shifting glacial dynamics and calving of sediment-laden icebergs from the smaller local Astrolabe and Zéléé outlet glaciers through this time.

There is a rapid increase in mud content at 4.5 ka coincident with a reduction in both the biogenic and terrigenous MARs, although the terrigenous MAR curve shows higher

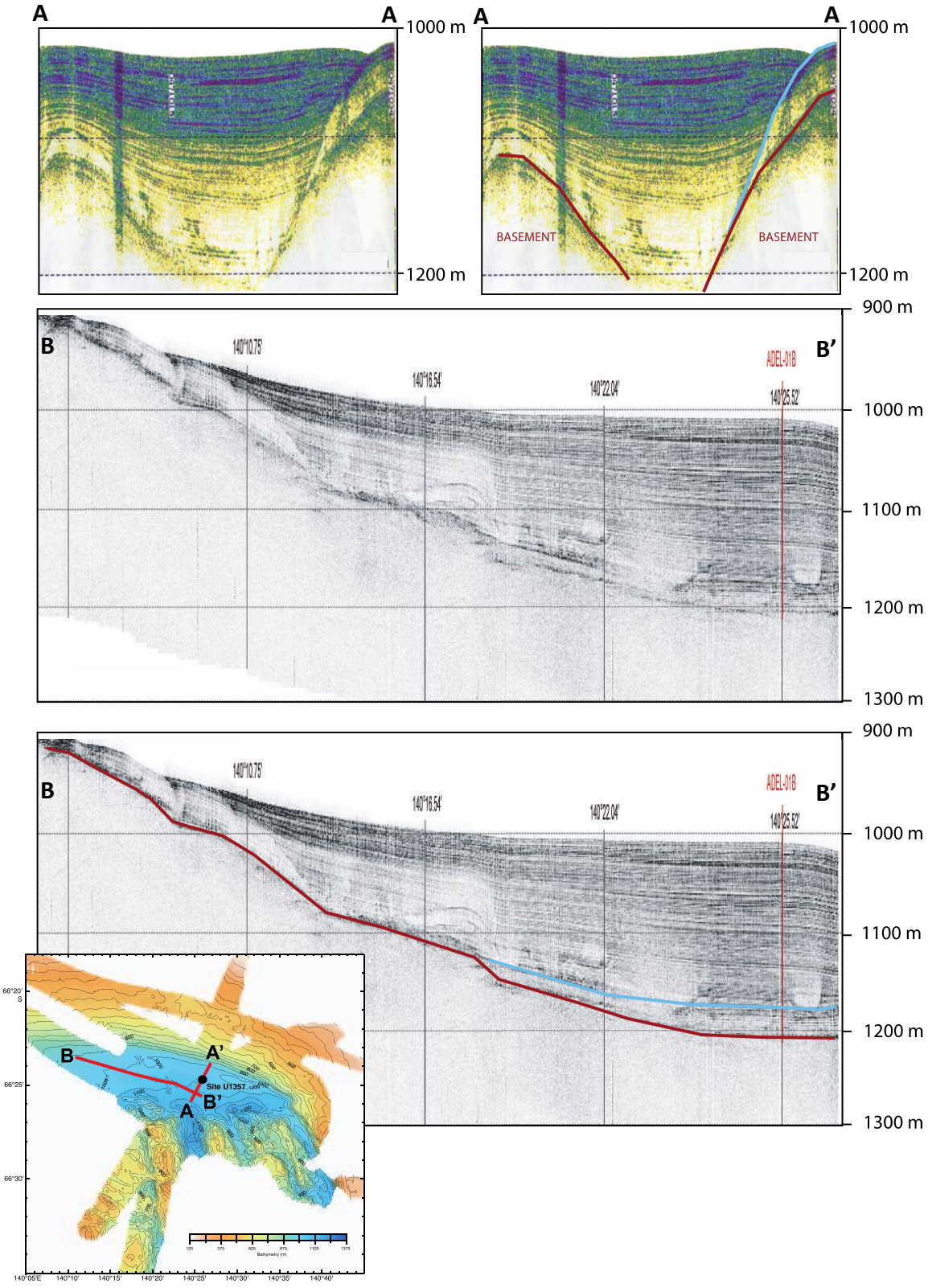

Figure S5 3.5 kHz seismic profile of the Adélie drift. Top: South (A) to north (A') profile, showing early Holocene (inferred to be ~11-8.2 ka) strata downlapping on top the basement highs (blue reflector and below). This is overlain by onlapping strata (blue reflector and above). Middle and Bottom: West (B) to East (B') profile, showing that in the depocentre of the basin, the pre-8.2 strata has a different geometry to overlying strata (onlapping onto the northern bank of the Dumont D'Urville Trough), suggesting a supply from the south, while overlying strata form a drift deposit that is thickest on the northern flank of the trough, and infers a drift deposit morphology that is aligned with the flow of easterly Antarctic Coastal Current.

accumulation rates than the biogenic MAR curve (Fig. S4). Hence, less material is being advected to the site, and the maximum current strength acting to winnow and advect material from the Adélie Bank into the Dumont d'Urville Trough is reduced. A reduction in maximum current strength could potentially be explained by more extensive sea ice over the site, which would act to reduce wind stress on the ocean surface and thus the maximum strength of the easterly flow, despite enhanced zonal easterly winds that are predicted with a cooler Antarctic climate (Shin et al., 2003; DeConto et al., 2007).

A final consideration is that aeolian contribution of terrigenous material is known to be of importance in Antarctic coastal areas affected by katabatic winds (Atkins and Dunbar, 2009; Chewings et al., 2014). However, windblown sediment is usually well-sorted, and combined with the lack of exposed sediment in Wilkes Land, and the distance of the core site from the coast, input of aeolian sediment into the ocean from melting sea ice is likely to be a relatively minor component of the sediment population relative to the suspended sediment load derived from the local banks and pelagic processes.

S2.3. Highly-branched isoprenoids (HBI)

Several recent studies have highlighted the strong potential of the HBI biomarkers along the Antarctic coast as a robust proxy of sea ice extent. Indeed, it has been shown that the di-unsaturated HBI lipid (i.e. diene II or $C_{25:2}$ alkene) is only synthesized in the modern Antarctic waters by sea ice-associated diatoms (Belt et al., 2016; Massé et al., 2011; Smik et al., 2016). The tri-unsaturated HBI lipid (i.e. triene III or $C_{25:3}$) is in contrast strictly produced by open water diatom species, which have been found to be in highest abundance in the marginal ice zone (Smik et al., 2016). Thus, the calculated diene/triene ratio is a reliable tracer to qualitatively estimate the sea ice extent (sea ice vs open water conditions). As previously applied in various Antarctic coastal sediments during different period of time (Etourneau et al., 2013; Collins et al., 2012; Barbara et al., 2010), the diene/triene

ratio was successfully used to reconstruct the past sea ice history around Antarctica. In particular, it has been shown that the HBIs were not significantly affected by (i) changes in sources (glacial ice vs sea ice), as the diatoms producing the HBIs strictly grow in relation with sea ice (under or at the edge) (ii) bacterial degradation (Robson and Rowland, 1988) or (iii) rapid sulfurization under anoxic conditions (Sinninghe Damsté et al., 2007). Absolute concentrations of the HBI diene and triene compounds are shown in Fig. S6.

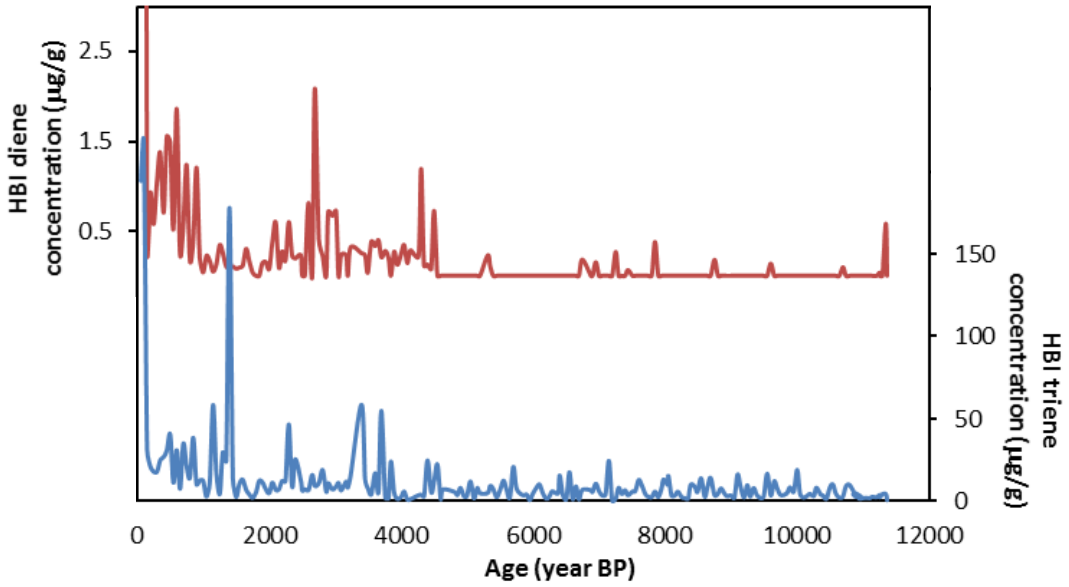

Figure S6 Absolute concentrations of highly branched isoprenoids (HBIs) measured in U1357B.

S3. Ross Sea deglaciation history

Our hypothesis is that large (cold) ice shelf cavity development south of Ross Island after ca. 6.5 and 4.5 ka was the driver of major changes in the surface water properties of the Ross Sea and offshore Adélie Land. The history of grounding line retreat to the north of Ross Island is relatively well-constrained, particularly in the Western Ross Sea, and the loss of residual ice caps appears to be largely complete by ca. 7 ka to the immediate north of Ross Island (Anderson et al., 2014; McKay et

al., 2016; Hall et al., 2004; Jones et al., 2015). Indeed, a phase of isotopically depleted glacial melt-water is apparent at Site U1357 between 8 and 7 ka and could be sourced from the Ross Sea, reconciling our model with these chronologies. Prior to 8 ka, any meltwater signal in U1357B is potentially influenced by local glacier retreat, based on the caveats noted earlier in the grainsize and geophysical datasets (S2.2), although we note a dominant Ross Sea contribution to this signal is possible.

To the south of Ross Island, we use the ice sheet retreat model of McKay et al. (2016) to help constrain the pattern and rate of retreat of the grounding line to the south of Ross Island. This was a higher resolution simulation of the (Golledge et al., 2014) model that applies a lower mantle viscosity that is more consistent with the West Antarctic sector of the continent, where the majority of ice loss occurred following the LGM. This allowed for more rapid glacio-isostatic adjustment, slowing down the marine ice sheet instability process, and helped significantly improve data model mismatches to the north of Ross Island. This model suggests that due to the bathymetric configuration of the Ross Sea, Holocene ice sheet retreat to the south of Ross Island is likely to be rapid and would have been completed by the mid-Holocene (ca. 5 ka).

Recent studies are converging on a rapid phase of retreat of the WAIS to its modern-day position (and potentially further south, followed by a short duration readvance of the grounding line) during the mid-Holocene (Hein et al., 2016; Spector et al., 2017; Kingslake et al., 2018). ^{10}Be exposure ages of erratics in coastal nunataks at the confluence of the Mercer Ice Stream and Reedy Glacier indicate 105 m of ice sheet deflation since 6.8 ka, with only 40 m of this after 4.9 ka (Todd et al., 2010), indicating a rapid phase of retreat between 6.8 ka and 4.9 ka. More recent deflation profiles for the Beardmore Glacier (84°S) and Scott Glacier (86°S) regions show sustained thinning between ca. 9 and 8 ka, but the Scott Glacier experience a second phase of rapid thinning of ca. 200 m between 6.8 and 5.3 ka (Fig. 2), followed by a slower rate of thinning of between 5.3 and 3.5 ka of ca. 100 m.

Ages younger than this, near the modern surface are thought to be related to surface ablation rather than dynamic thinning. This suggests that the grounding line was at its modern location by ca. 3.5 ka (Spector et al., 2017). Glaciological evidence from radar profiles suggests the development of divide flow on Roosevelt Island occurred sometime between 3 and 4 ka BP, suggesting that the ice sheet thickness was at least 500 m thicker until this time (Conway et al., 1999).

Combined, these lines of evidence suggest the majority of grounding line retreat south of Ross Island occurred after 8 ka, with a sustained retreat occurring after 6.8 ka, consistent with the timing of the glacial meltwater feeding the U1357 site. Most evidence suggest thinning of the outlet glaciers was rapid, and the grounding line was near its modern day position sometime between 4.5 and 3.4 ka. A slighter younger age (e.g. 3 – 3.5 ka) for final establishment of the modern grounding line position is consistent with our interpretation, as we suggest a threshold for ice shelf cavity development was reached at 4.5 ka, whereby ice shelf-ocean interactions lead to the initiation of the negative sea ice feedbacks. However as discussed in the main text, this negative feedback may have acted to slow and stabilise retreat by ca. 3 – 3.5 ka, and values of δ^2H do not stabilize in U1357B until ca. 3 ka. Thus we infer this was the consequence of the final cessation of significant glacial meltwater source from Ross Sea retreat, noting the timing difference and the range of numerous uncertainties associated with these records, including radiocarbon reservoir ages and production rates for the cosmogenic data.

S4. Data-Model mismatch

Comparison of sea ice data from the Adélie region (presented in this study), with model output for sea ice thickness and extent from TraCE-21k simulations, indicates a clear mismatch between the observational data and model output over the Holocene (Fig. S7). The rapid mid-Holocene increase in sea ice, recorded at Site U1357 and other sites in the Antarctic coastal zone (Fig. S7c, d), is not seen in the model simulations, which instead indicate a sharp decline in sea ice extent and thickness around the Antarctic and in the Adélie region after ca. 5 ka (Fig. S7a, b). The Community Climate

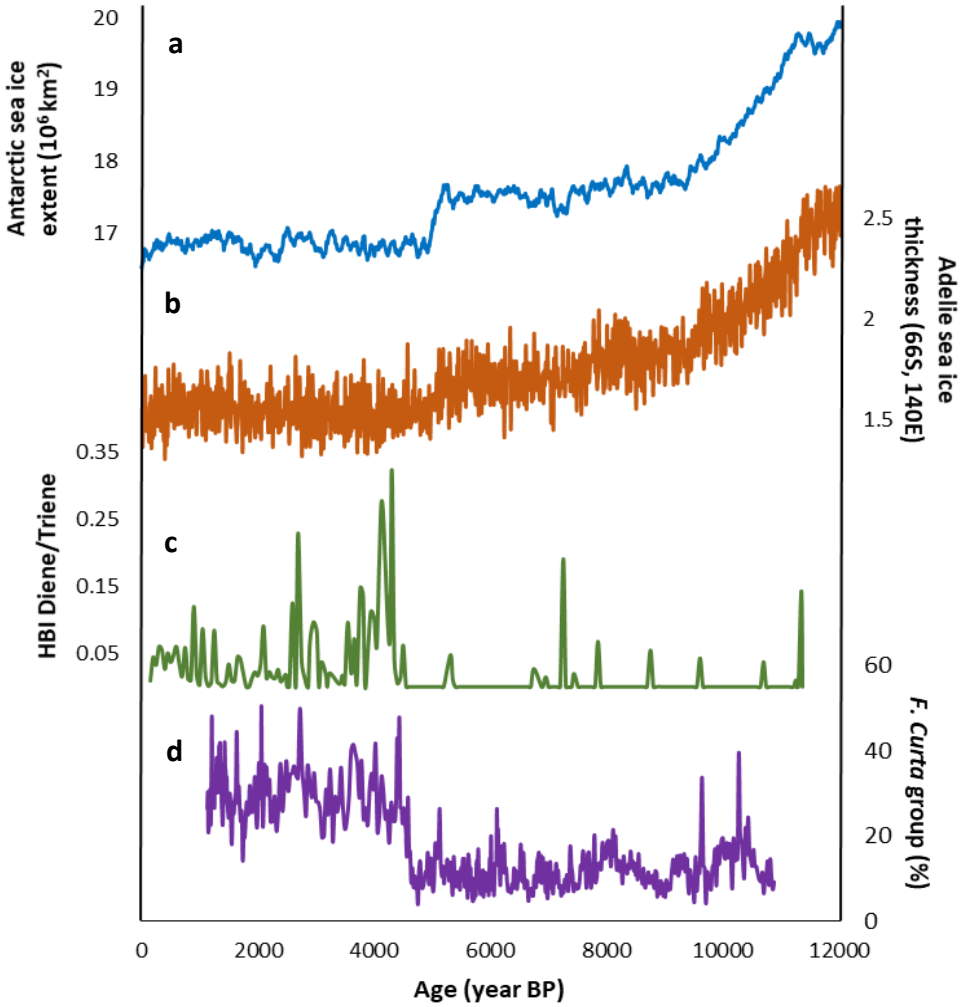

Figure S7 Comparison of sea ice data from the Adélie region with TraCE-21k simulations a) Antarctic sea ice extent (10^6 km^2) from TraCE-21k b) Adélie sea ice thickness (66°S, 140°E) from TraCE-21k c) Ratio of the di-unsaturated HBI (C25:2; Diene) and the tri-unsaturated HBI isomer (C25:3; Triene) at Site U1357 d) *Fragilariopsis curta* group relative abundances from MD03-2601.

System Model (CCSM3) used in the simulations lacks a dynamic ice sheet, instead using a constant prescribed meltwater flux of 1.12 m ka^{-1} from the Antarctic which finishes at 5 ka, which can likely

explain the simulated sea-ice decline at ca. 5 ka. Furthermore, it does not incorporate ice-ocean coupling or ice shelf cavities. We have shown that these processes have an important role on sea ice production and thus are required within models to capture the coupled response between ice sheets and the ocean. We note that some models, such as LOVECLIM (Renssen et al., 2010), do simulate a gradual sea-ice increase and cooling trend in the late Holocene, however the timing (gradual) and magnitude (subtle) of sea-ice trends do not match the abrupt and large changes seen in the proxy data.

Supplementary information references

Anderson, J.B., Conway, H., Bart, P.J., et al. (2014) Ross Sea paleo-ice sheet drainage and deglacial history during and since the LGM. *Quaternary Science Reviews*, 100: 31–54. doi:10.1016/j.quascirev.2013.08.020.

Andrews, J.T., Domack, E.W., Cunningham, W.L., et al. (1999) Problems and possible solutions concerning radiocarbon dating of surface marine sediments, Ross Sea, Antarctica. *Quaternary Research*, 52 (2): 206–216. doi:10.1006/qres.1999.2047.

Atkins, C.B. and Dunbar, G.B. (2009) Aeolian sediment flux from sea ice into Southern McMurdo Sound, Antarctica. *Global and Planetary Change*, 69 (3): 133–141. doi:10.1016/j.gloplacha.2009.04.006.

Bahr, A., Jiménez-Espejo, F.J., Kolasinac, N., et al. (2014) Deciphering bottom current velocity and paleoclimate signals from contourite deposits in the Gulf of Cádiz during the last 140 kyr: An inorganic geochemical approach. *Geochemistry, Geophysics, Geosystems*, 15 (8): 3145–3160. doi:10.1002/2014GC005356.

Barbara, L., Crosta, X., Massé, G., et al. (2010) Deglacial environments in eastern Prydz Bay, East Antarctica. *Quaternary Science Reviews*, 29 (19–20): 2731–2740. doi:10.1016/j.quascirev.2010.06.027.

Beaman, R.J., O'Brien, P.E., Post, A.L., et al. (2011) A new high-resolution bathymetry model for the Terre Adélie and George V continental margin, East Antarctica. *Antarctic Science*, 23 (1): 95–103. doi:10.1017/S095410201000074X.

Belt, S.T., Smik, L., Brown, T.A., et al. (2016) Source identification and distribution reveals the potential of the geochemical Antarctic sea ice proxy IPSO25. *Nature Communications*, 7: 12655. doi:10.1038/ncomms12655.

Bentley, M.J., Ocofaigh, C., Anderson, J.B., et al. (2014) A community-based geological reconstruction of Antarctic Ice Sheet deglaciation since the Last Glacial Maximum. *Quaternary Science Reviews*, 100: 1–9. doi:10.1016/j.quascirev.2014.06.025.

Blaauw, M. and Christeny, J.A. (2011) Flexible paleoclimate age-depth models using an autoregressive gamma process. *Bayesian Analysis*, 6 (3): 457–474. doi:10.1214/11-BA618.

Chewings, J.M., Atkins, C.B., Dunbar, G.B., et al. (2014) Aeolian sediment transport and deposition in a modern high-latitude glacial marine environment. *Sedimentology*, 61 (6): 1535–1557. doi:10.1111/sed.12108.

Collins, L.G., Pike, J., Allen, C.S., et al. (2012) High-resolution reconstruction of southwest Atlantic sea-ice and its role in the carbon cycle during marine isotope stages 3 and 2. *Paleoceanography*, 27 (3). doi:10.1029/2011PA002264.

Conway, H., Hall, B.L., Denton, G.H., et al. (1999) Past and Future Grounding-Line Retreat of the West Antarctic Ice Sheet. *Science*, 286 (5438): 280–283. doi:10.1126/science.286.5438.280.

Crosta, X., Denis, D. and Ther, O. (2008) Sea ice seasonality during the Holocene, Adelie Land, East Antarctica. *Marine Micropaleontology*, 66 (3–4): 222–232. doi:10.1016/j.marmicro.2007.10.001.

DeConto, R., Pollard, D. and Harwood, D. (2007) Sea ice feedback and Cenozoic evolution of Antarctic climate and ice sheets. *Paleoceanography*, 22 (3). doi:10.1029/2006PA001350.

Denis, D., Crosta, X., Schmidt, S., et al. (2009a) Holocene glacier and deep water dynamics, Adélie Land region, East Antarctica. *Quaternary Science Reviews*. doi:10.1016/j.quascirev.2008.12.024.

Denis, D., Crosta, X., Schmidt, S., et al. (2009b) Holocene productivity changes off Adélie land (East Antarctica). *Paleoceanography*, 24 (3): 1–12. doi:10.1029/2008PA001689.

Dunbar, R.B., Anderson, J.B., Domack, E.W., et al. (1985) "Oceanographic influences on sedimentation along the Antarctic continental shelf." In *Oceanology of the Antarctic Continental Shelf (eds S. Jacobs)*. pp. 291–312. doi:10.1029/AR043p0291.

Escutia, C., Brinkhuis, H. and Klaus, A. (2011) Site summary. *Proc. IODP* |, 318: 1–74. doi:10.2204/iodp.proc.318.105.2011.

Etourneau, J., Collins, L.G., Willmott, V., et al. (2013) Holocene climate variations in the western Antarctic Peninsula: Evidence for sea ice extent predominantly controlled by changes in insolation and ENSO variability. *Climate of the Past*, 9 (4): 1431–1446. doi:10.5194/cp-9-1431-2013.

Folk, R.L. and Ward, W.C. (1957) Brazos River bar [Texas]; a study in the significance of grain size parameters. *Journal of Sedimentary Research*, 27 (1): 3–26. doi:10.1306/74D70646-2B21-11D7-8648000102C1865D.

Golledge, N.R., Menviel, L., Carter, L., et al. (2014) Antarctic contribution to meltwater pulse 1A from reduced Southern Ocean overturning. *Nature communications*, 5: 5107. doi:10.1038/ncomms6107.

Griffith, E.M. and Paytan, A. (2012) Barite in the ocean - occurrence, geochemistry and palaeoceanographic applications. *Sedimentology*, 59 (6): 1817–1835. doi:10.1111/j.1365-3091.2012.01327.x.

Hall, B.L., Baroni, C. and Denton, G.H. (2004) Holocene relative sea-level history of the Southern Victoria Land Coast, Antarctica. *Global and Planetary Change*, 42 (1–4): 241–263. doi:10.1016/j.gloplacha.2003.09.004.

Hall, B.L., Henderson, G.M., Baroni, C., et al. (2010) Constant Holocene Southern-Ocean14C reservoir ages and ice-shelf flow rates. *Earth and Planetary Science Letters*, 296 (1–2): 115–123. doi:10.1016/j.epsl.2010.04.054.

Hein, A.S., Marrero, S.M., Woodward, J., et al. (2016) Mid-Holocene pulse of thinning in the Weddell Sea sector of the West Antarctic ice sheet. *Nature Communications*, 7: 12511. doi:10.1038/ncomms12511.

Jones, R.S., Mackintosh, A.N., Norton, K.P., et al. (2015) Rapid Holocene thinning of an East Antarctic outlet glacier driven by marine ice sheet instability. *Nature Communications*, 6: 8910. doi:10.1038/ncomms9910.

Kingslake, J., Scherer, R.P., Albrecht, T., et al. (2018) Extensive retreat and re-advance of the West Antarctic Ice Sheet during the Holocene. *Nature*, 558 (7710): 430–434. doi:10.1038/s41586-018-0208-x.

Kleinschmidt, G. and Talarico, F. (2000) The Mertz shear zone. *Terra Antarctica Reports*, pp. 109–115.

Massé, G., Belt, S.T., Crosta, X., et al. (2011) Highly branched isoprenoids as proxies for variable sea ice conditions in the Southern Ocean. *Antarctic Science*, 23 (5): 487–498. doi:10.1017/S0954102011000381.

Massom, R.A., Hill, K.L., Lytle, V.I., et al. (2001) Effects of regional fast-ice and iceberg distributions on the behaviour of the Mertz Glacier polynya, East Antarctica. *Annals of Glaciology*, 33: 391–398. doi:10.3189/172756401781818518.

McCave, I.N. and Hall, I.R. (2006) Size sorting in marine muds: Processes, pitfalls, and prospects for paleoflow-speed proxies. *Geochemistry, Geophysics, Geosystems*, 7 (10). doi:10.1029/2006GC001284.

McKay, R., Browne, G., Carter, L., et al. (2009) The stratigraphic signature of the late Cenozoic Antarctic Ice Sheets in the Ross Embayment. *Bulletin of the Geological Society of America*, 121 (11–12): 1537–1561. doi:10.1130/B26540.1.

McKay, R., Golledge, N.R., Maas, S., et al. (2016) Antarctic marine ice-sheet retreat in the Ross Sea during the early Holocene. *Geology*, 44 (1): 7–10. doi:10.1130/G37315.1.

Paytan, A., Mearon, S., Cobb, K., et al. (2002) Origin of marine barite deposits: Sr and S isotope characterization. *Geology*, 30 (8): 747–750. doi:10.1130/0091-7613(2002)030<0747:OOMBDS>2.0.CO;2.

Plewa, K., Meggers, H. and Kasten, S. (2006) Barium in sediments off northwest Africa: A tracer for paleoproductivity or meltwater events? *Paleoceanography*, 21 (2): 1–15. doi:10.1029/2005PA001136.

Powell, R. and Domack, E. (1995) "Glaciomarine processes and sediments." In *Modern Glacial Environments (Eds J. Menzies)*. Butterworth-Heinemann, Oxford.

Presti, M., Barbara, L., Denis, D., et al. (2011) Sediment delivery and depositional patterns off Adélie Land (East Antarctica) in relation to late Quaternary climatic cycles. *Marine Geology*, 284 (1–4): 96–113. doi:10.1016/j.margeo.2011.03.012.

Renssen, H., Goosse, H., Crosta, X., et al. (2010) Early holocene laurentide ice sheet deglaciation causes cooling in the high-latitude southern hemisphere through oceanic teleconnection. *Paleoceanography*, 25 (3): 1–15. doi:10.1029/2009PA001854.

Robson, J.N. and Rowland, S.J. (1988) Biodegradation of highly branched isoprenoid hydrocarbons: A possible explanation of sedimentary abundance. *Organic Geochemistry*, 13 (4–6): 691–695. doi:10.1016/0146-6380(88)90090-3.

Shin, S.-I., Liu, Z., Otto-Bliesner, B.L., et al. (2003) Southern Ocean sea-ice control of the glacial North Atlantic thermohaline circulation. *Geophysical Research Letters*, 30 (2). doi:10.1029/2002GL015513.

Singer, J.K. and Anderson, J.B. (1984) Use of total grain-size distributions to define bed erosion and transport for poorly sorted sediment undergoing simulated bioturbation. *Marine Geology*, 57 (1–4): 335–359. doi:10.1016/0025-3227(84)90204-4.

Sinninghe Damsté, J.S., Rijpstra, W.I.C., Coolen, M.J.L., et al. (2007) Rapid sulfurisation of highly branched isoprenoid (HBI) alkenes in sulfidic Holocene sediments from Ellis Fjord, Antarctica. *Organic Geochemistry*, 38 (1): 128–139. doi:10.1016/j.orggeochem.2006.08.003.

Smik, L., Belt, S.T., Lieser, J.L., et al. (2016) Distributions of highly branched isoprenoid alkenes and other algal lipids in surface waters from East Antarctica: Further insights for biomarker-based paleo sea-ice reconstruction. *Organic Geochemistry*, 95: 71–80. doi:10.1016/j.orggeochem.2016.02.011.

Spector, P., Stone, J., Cowdery, S.G., et al. (2017) Rapid early-Holocene deglaciation in the Ross Sea, Antarctica. *Geophysical Research Letters*, 44 (15): 7817–7825. doi:10.1002/2017GL074216.

Thomas, D.N. (2011) "Biogeochemistry of Sea Ice." In *Encyclopedia of Snow, Ice and Glaciers (eds Singh V.P., Singh P., Haritashya U.K.)*. pp. 98–102. doi:10.1007/978-90-481-2642-2_639.

Thomas, R.H. and Bentley, C.R. (1978) A model for Holocene retreat of the West Antarctic Ice Sheet. *Quaternary Research*, 10 (2): 150–170. doi:10.1016/0033-5894(78)90098-4.

Todd, C., Stone, J., Conway, H., et al. (2010) Late Quaternary evolution of Reedy Glacier, Antarctica. *Quaternary Science Reviews*, 29 (11–12): 1328–1341. doi:10.1016/j.quascirev.2010.02.001.